Corrosion fatigue behavior of additively manufactured biodegradable porous iron

Li, Yageng; Lietaert, K.; Li, Wei; Zhang, X.Y.; Leeflang, M. A.; Zhou, Jie; Zadpoor, A. A.

DOI
10.1016/j.corsci.2019.05.003

Publication date
2019

Document Version
Accepted author manuscript

Published in
Corrosion Science

Citation (APA)
Li, Y., Lietaert, K., Li, W., Zhang, X. Y., Leeflang, M. A., Zhou, J., & Zadpoor, A. A. (2019). Corrosion fatigue behavior of additively manufactured biodegradable porous iron. *Corrosion Science*, *156*, 106-116. https://doi.org/10.1016/j.corsci.2019.05.003

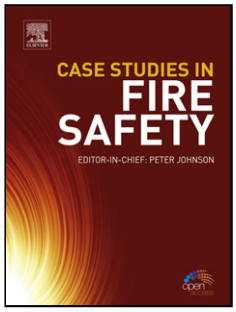

Title: Corrosion fatigue behavior of additively manufactured biodegradable porous iron

Authors: Y. Li, K. Lietaert, W. Li, X-Y. Zhang, M.A. Leeflang, J. Zhou, A.A. Zadpoor

PII: S0010-938X(19)30240-9
DOI: https://doi.org/10.1016/j.corsci.2019.05.003
Reference: CS 8011

To appear in:

Received date: 31 January 2019
Revised date: 11 April 2019
Accepted date: 6 May 2019

Please cite this article as: Li Y, Lietaert K, Li W, Zhang X-Y, Leeflang MA, Zhou J, Zadpoor AA, Corrosion fatigue behavior of additively manufactured biodegradable porous iron, *Corrosion Science* (2019), https://doi.org/10.1016/j.corsci.2019.05.003

Original paper

Corrosion fatigue behavior of additively manufactured biodegradable porous iron

Y. Li[1*], K. Lietaert [2,3], W. Li[4], X-Y. Zhang[5], M.A. Leeflang[1], J. Zhou[1#], A.A. Zadpoor[1#]

[1]*Department of Biomechanical Engineering, Delft University of Technology, Delft 2628 CD, The Netherlands*

[2]*3D Systems - LayerWise NV, Grauwmeer 14, Leuven 3001, Belgium*

[3] *Department of Materials Engineering, KU Leuven, Kasteelpark Arenberg 44, Leuven 3001, Belgium*

[4]*Department of Materials Science and Engineering, Delft University of Technology, Delft 2628 CD, The Netherlands*

[5]*Department of Mechanical Engineering, Tsinghua University, Beijing 10004, China*

[#]Authors contributed equally to the study.

[*]Corresponding author, E-mail: y.li-7@tudelft.nl.

Tel: +31-15-2786780.

Highlights

1. This is the first study about the corrosion fatigue behavior of selective laser melted (SLM) biodegradable porous iron based on diamond unit cells. A novel test setup was developed that complemented the fatigue test machine and ensured that cyclic loading on the specimen could occur in circulated r-SBF at 37 ^{o}C.

2. AM porous iron exhibited high fatigue resistance with fatigue strengths being 70% and 65% of yield stress in air and revised simulated body fluid (r-SBF), respectively.

3. How biodegradation and cyclic loading affected each other were investigated at both macro and micro scales. The observed high fatigue strength and slow biodegradation rate underline the importance of AM porous iron as a promising bone-substituting material.

Abstract

The corrosion fatigue behavior of additively manufactured topologically ordered porous iron based on diamond unit cells was studied for the first time to understand its response to cyclic loading in a simulated physiological environment. The material exhibited high fatigue resistance with fatigue strengths being 70% and 65% of yield stress in air and revised simulated body fluid, respectively, mainly due to its slow degradation and excellent ductility. However, cyclic loading significantly increased biodegradation rate, especially at higher stress levels. The observed extraordinary fatigue strength, slow biodegradation and high ductility underline the importance of porous iron as a promising bone-substituting material.

Keywords: Additive manufacturing; selective laser melting; iron scaffold; corrosion fatigue; biodegradation.

1. INTRODUCTION

Additively manufactured (AM) bio-inert porous metals, such as titanium, stainless steel, and cobalt-chromium alloys, have been excessively studied as promising materials for orthopedic implants over the last few years [1-5]. AM provides a unique possibility to precisely control the freeform topology of such biomaterials, which presents an unparalleled opportunity, given that it allows for tailoring the mechanical properties of porous structures so as to mimic those of the human bone [6]. Moreover, the interconnected pores of topologically ordered porous biomaterials support cell proliferation and propagation [7]. However, bio-inert metallic implants permanently stay in the body, which is not ideal, especially for young patients [8]. Even for the adult patient population, there is always a risk that a second surgery is needed, particularly when chronic local inflammatory reactions occur [9].

Using biodegradable metals, such as magnesium, iron, and zinc alloys, could address the above-mentioned limitation of bio-inert porous metals by adding biodegradability to the already impressive list of the advantages that AM porous metallic biomaterials offer. Despite their distinct advantages, there were only a few studies on the development of AM biodegradable metallic scaffolds for orthopedic applications and electrodeposition [10], ink/binder-jetting [11-13] have been used. It is, however, difficult (if not impossible) to use these methods to create fully interconnected porous structures with complex external shapes and intricate internal architectures in combination with adequate stiffness and strength. The first reports of applying selective laser melting (SLM) to fabricate topologically ordered biodegradable porous metals, such as magnesium and iron [14, 15], have just appeared in the literature. The quasi-static mechanical properties of those topologically ordered AM porous metals have been found to remain in the range of the values reported for trabecular bone even after 4 weeks of *in vitro* biodegradation [14, 15].

Quasi-static mechanical properties alone are, however, not enough for understanding how biomaterials function under physiological load. Bone-substituting biomaterials including AM biodegradable porous metals are expected to undergo millions of cycles of mechanical loading [16, 17], and may therefore experience fatigue fracture, even when the maximum stress experienced by the material is less than its yield stress. In the case of biodegradable metals, the complexity of understanding the dynamic nature of the fatigue behavior is compounded by the fact that biodegradation and fatigue mutually affect each other. Moreover, both the topological design of the porous structure and material type affect the fatigue behavior of AM porous biomaterials, even for bio-inert metals [2]. Taken together, the isolated and coupled effects of all above-mentioned factors make for a complex multi-factorial biodegradation-, topology- and material-dependent fatigue phenomenon that requires a detailed systematic study to unravel. The research on the fatigue behavior of AM biodegradable porous metals has just begun with one single study on AM porous magnesium (the WE43 magnesium alloy) [18]. No comparable studies exist for AM porous iron or for any other type of biodegradable porous metals.

In this paper, we present the results of the first study ever on the fatigue behavior of AM porous iron. As the major mode of loading in orthopedic porous implant is compression [19], the compression-compression loading mode was chosen for this work. In particular, we carefully designed our study so as to understand some of the above-mentioned aspects regarding the fatigue behavior of AM biodegradable porous metals and to distinguish between the roles of different factors. The topological design was, for example, kept constant (*i.e.*, being similar to the previous study on magnesium) to decouple the effect of material type on corrosion-fatigue behavior from that of topological design. We performed all our experiments both in air and in revised simulated body fluid (r-SBF) using a novel test setup that complemented our fatigue test machine and ensured that cyclic loading on the specimen

could occur in circulated r-SBF at 37 ºC [20]. This parallel design of the study allowed us to investigate the mutual effects of biodegradation and cyclic loading on each other.

2. MATERIAL AND METHODS

2.1. Scaffold manufacturing and post processing

Iron scaffolds with diamond unit cells (a strut thickness of 200 µm and a unit cell size of 1 mm) were designed by using Magics (Materialise, Belgium) to have a height of 10.5 mm, a diameter of 10 mm and a relative density of 20% (Fig. 1a and b). A ProX DMP 320 machine (3D Systems, Belgium) with the DMP Suite software (3D Systems, Belgium) was used for direct metal printing of the samples using the selective laser melting (SLM) technique. We used a nitrogen gas atomized Fe powder (Material Technology Innovations Co., Ltd., China) (Fig. 1c) with the following characteristics: purity: 99.88%; particle sizes: D_{10}=32 µm, D_{50}=48 µm, and D_{90}=71 µm; morphology: spherical; apparent density: 4.09 g/cm^3; tap density: 4.88 g/cm^3; angle of repose: 157 °; carbon content: 0.0044%. The powder was deposited in layers of 30 µm thick. Only contours but no hatch vectors were used (0.33 W/mm energy density) during the printing process. The samples were built on a steel base plate and later on removed by means of electrical discharge machining (EDM). Powder particles entrapped in pores were removed through ultrasonic cleaning in 96 % ethanol for 20 min. Then, the samples were chemically cleaned in 50% HCl for 1 min to remove residuals from EDM and loose powder particles, followed by 5 min ultrasonic cleaning in 96% ethanol to wash out HCl. The bulk density of AM porous iron and the porosity within the struts were determined using the Archimedes' method.

2.2. Characterization of microstructure

Electron back-scattered diffraction (EBSD) data were collected using an HKL Nordlys II detector at a step size of 200 nm attached to a JEOL JSM-6500F field emission gun scanning electron microscope (FEGSEM). Image quality (IQ) and inverse pole figure (IPF) maps were

reconstructed by using the commercial software TSL OIM® Analysis. Samples for EBSD analysis were prepared by grinding, mechanical polishing up to 1 μm diamond abrasives in liquid suspension, and further mechanical polishing using 0.04 μm silica oxide.

2.3. Fatigue tests in air and in r-SBF

Compression-compression fatigue tests were performed at a minimum to maximum stress ratio of 0.1, a frequency of 15 Hz, and six different stress levels (maximum stress): $0.65\sigma_y$, $0.7\sigma_y$, $0.75\sigma_y$, $0.8\sigma_y$, $0.85\sigma_y$ and $0.9\sigma_y$, where σ_y is the yield stress (=28 MPa [15]) using an electro-dynamic mechanical testing machine (Instron E10000 ElectroPlus with a 10 kN load cell). The tests were stopped when specimens failed, unless failure did not occur until 3×10^6 loading cycles (which lasted 2.3 days). The stress applied without causing failure after 3×10^6 loading cycles is defined as fatigue strength. Corrosion fatigue tests were performed by using the same machine equipped with a double-wall specimen chamber designed and manufactured in-house (Fig. 1c). Corundum was used as the material of the compression head. The specimen was immersed in 300 ml circulated r-SBF [20] inside the chamber throughout the test. The temperature of r-SBF was held at 37 °C and the flow rate was controlled at 1.2 ml/min [21] with a peristaltic pump. Purging of CO_2 at 5% was maintained during the test. The ratcheting strain rate [22] per cycle was calculated as $d[(\varepsilon_{max} + \varepsilon_{min})/2]/dN$, where ε_{max} and ε_{min} are the maximum and minimum axial strains in a cycle, respectively, and N is the number of cycles. The influence of biodegradation on the fatigue strength was evaluated by the reduction ratio of fatigue strength (RRFS) [17], *i.e.*, $(\sigma_{Air} - \sigma_{SBF})/\sigma_{Air}$, where σ_{Air} and σ_{SBF} are the fatigue strength in air and in r-SBF, respectively. Iron (ρ_{Fe}), calcium and phosphate ion concentration in the r-SBF solution was determined using an inductively coupled plasma optical emission spectroscope (ICP-OES, iCAP 6500 Duo, Thermo Scientific). Then, the biodegradation rate was calculated based on the iron ion

concentration data: $v_{br}=(\rho_{Fe}\times V)/t$, where V is the volume of the r-SBF and t the immersion time. All the tests were performed in triplicates for each stress level.

2.4. Static immersion tests in r-SBF

Static immersion tests were carried out in 300 ml r-SBF at 37 °C without any mechanical loading for comparison purposes. The immersion time was in accordance with that of the corrosion fatigue tests at three stress levels: $0.65\sigma_y$ (55.5 h), $0.75\sigma_y$ (5.5 h), and $0.9\sigma_y$ (1 h). Ion concentration and biodegradation rate was determined similarly as mentioned above in section 2.3. All the tests were performed in triplicates for each immersion time.

2.5. Characterization of corrosion products

The morphologies and compositions of the corrosion products on the surface of the specimens after the biodegradation tests with and without cyclic loading were analyzed with a scanning electron microscope (SEM) equipped with energy-dispersive X-ray spectroscopy (EDS) (SEM, JSM-IT100, JEOL). An accelerating voltage of 15 kV was used for the EDS analyses.

2.6. Characterization of crack morphology and distribution

The morphologies of the cracks appearing after the corrosion fatigue tests were examined using a SEM (JSM-IT100, JEOL). EBSD analysis was performed to reveal the grain orientations around the cracks. The first nearest-neighbor Kernel Average Misorientation (KAM) maps, calculated from EBSD data, was chosen to represent the local misorientations.

After the fatigue tests, the specimens were mounted in resin and polished up to 1 μm diamond abrasives in liquid suspension. A Keyence VHX5000 digital microscope was used to observe fatigue crack distribution on the cross section of the entire specimen.

2.7. Finite element (FE) modeling

Simulations with the finite element method (FEM) were conducted using the commercial software package Abaqus (Dassault System Simulia Corp, France) to study the stress

distribution in the fatigue specimens. Single diamond unit cell was developed as the representative volume elements (RVE) of the porous structure. The RVE models were subjected to a compressive load of $0.65\sigma_y$. The contours of the first principal stress of the RVE models were extracted to study stress concentrations.

2.8. Characterization of strain accumulation

X-ray diffraction (XRD) pattern was generated by using an X-ray diffractometer (Bruker D8 Advance diffractometer in Bragg-Brentano geometry). The diffractometer was equipped with a graphite monochromator and Vantec position sensitive detector and operated at 45 kV and 35 mA with a step size of 0.0214° and a dwell time of 3 s per step using Co Ka radiation. The top surface of the scaffold was aligned with the goniometer axis. The struts on the top were aligned with the direction of the X-ray beam. The full width at half maximum (FWHM) was determined using the "Create Area" function of the Bruker-Eva software. The XRD analysis was performed in triplicates.

2.9. Statistical analysis

Differences in biodegradation rate between the groups with and without cyclic loading were analyzed using one-way analysis of variance (ANOVA), followed by *post-hoc* Turkey test. A *p*-value below 0.05 was assumed to indicate a statistically significant difference ($p < 0.05$, *; *n.s.* = not significant).

3. RESULTS

3.1. Porosity and microstructural features of the AM iron scaffolds

The bulk porosity of the AM iron scaffolds was 73.2 ± 0.1%. Th porosity within the struts was determined to be 0.8% ± 0.1%. Melt lines were not visible on the cross section of SLM iron scaffold struts (Fig. 2a). Only several elongated grains along the length of the strut were observable. The microstructures of the SLM iron scaffolds were featured by a combination of mostly equiaxed fine grains, several irregular large grains and ultra-fine grains. IPF mapping

and pole figures (PF) showed that the grains had no preferred growth orientation (Fig. 2b and c).

3.2. Degradation-affected fatigue behavior

Strain ratcheting rate increased with increasing stress level both in air and in r-SBF (Fig. 3a). However, at the same stress level, the strain ratcheting rates of fatigue specimens in air and in r-SBF overlapped with each other. The S-N curves showed that the fatigue strength of the AM iron scaffolds decreases from $0.7\sigma_y$ in air to $0.65\sigma_y$ in r-SBF (Fig. 3b). Thus, the RRFS of the AM iron scaffolds was 0.08.

At the macro-scale, there were no visual differences between the fatigue specimens tested in air and in r-SBF (Fig. 3c). At 2% strain before failure, neither the specimens tested in air nor the ones tested in r-SBF showed any obvious visual changes (from outside). Even at 5% strain, no fracture plane was observable under either condition (Fig. 3c). Instead, the structure of the iron scaffolds slipped slightly sideways (Fig. 3c).

3.3. Fatigue-affected degradation behavior

The biodegradation rates of all specimens tested under cyclic loading increased as compared to those of the specimens subjected to static immersion tests (Fig. 3d). The increase was more significant at a higher stress level (compare the corrosion rates at *e.g.*, $0.75\sigma_y$ and $0.9\sigma_y$). Moreover, the biodegradation rate increased with rising stress level (Fig. 3d).

Under cyclic loading, both Ca and P ion concentrations in r-SBF were lower than those in static immersion (Fig. 3e and f). For the Ca ion concentration, the differences were significant at $0.65\sigma_y$ and $0.75\sigma_y$, while for the P ion concentration, the differences were significant at $0.65\sigma_y$ and $0.9\sigma_y$.

EDS analysis revealed that the corrosion products all contained C, O, P, Ca and Fe elements. At the same immersion time, specimens under cyclic loading had higher P and Ca contents in their corrosion products (Fig. 4). Moreover, pits, as a result of localized degradation, were

only found on iron scaffold struts subjected to cyclic loading (Fig. 4b, d and f), while the degradation of iron struts without mechanical loading occurred uniformly (Fig. 4a, c and e).

3.4. Fatigue crack distribution and characterization

Under $0.9\sigma_y$ cyclic loading, at 2% strain, cracks initiated mostly at the strut junctions and were distributed randomly within the whole scaffolds (Fig. 5a and b). There was no obvious increase in the number of cracks in the specimens tested in r-SBF as compared to that tested in air. At 5% strain, the cracks became wider and longer (Fig. 5c and d). However, no cracks that had propagated through the entire strut were found. The failure modes of the specimens tested in air and in r-SBF were similar. Under cycling loading, struts were still interconnected while several layers of struts in the middle of the specimens glided (Fig. 5c and d). At $0.65\sigma_y$, although the specimen did not fail after 3×10^6 loading cycles both in air and in r-SBF, cracks in the scaffolds had already initiated (Fig. 5e and f). Unlike fatigue tests at the highest stress level (i.e., $0.9\sigma_y$), more cracks had initiated in the specimens tested in r-SBF than those tested in air (compare Fig. 5e and f).

From the SEM images of crack morphology, it could be inferred that cracks preferentially initiated from the surface at the junction of struts both for the specimens tested in air and for those tested in r-SBF (Fig. 6). At $0.9\sigma_y$, cracks coexisted with pits that were formed as a result of localized degradation (Fig. 6f). At $0.65\sigma_y$, no cracks in the specimens tested in air were observed. In r-SBF, however, pits as a result of localized degradation near the cracks were found, being similar to the specimens subjected to cyclic loading at $0.9\sigma_y$ (Fig. 6i).

FE modeling indicated tensile stresses being concentrated at the strut junctions, while compressive stresses were present mostly in the body of the struts (Fig. 6j).

EBSD analysis showed the crack propagation to be transgranular (Fig. 7a and b). Moreover, there were no preferred orientations of the cracks with respect to the grains (Fig. 7b). KAM maps indicated that there were more concentrations of maximum average intragranular

misorientations around the cracks in the fatigue specimens tested under $0.9\sigma_y$ cyclic loading than those subjected to $0.65\sigma_y$ cyclic loading and in the as-built specimens (Fig. 7c, d and e). Obviously, these disorientations did not develop to such an extent that grain splitting was activated.

3.5. FWHM of the iron scaffolds

XRD showed no marked differences in peak intensity between the specimens before and after the fatigue tests at 0.65 and $0.9\sigma_y$ (Fig. 8a). However, FWHM slightly increased after the fatigue test at $0.9\sigma_y$ (Fig. 8b), while at $0.65\sigma_y$, FWHM remained almost the same as the as-built specimen at low Bragg angles. Interestingly, the FWHM values even decreased at high Bragg angles (Fig. 8b).

4. DISCUSSION

For the first time ever, we systematically studied the fatigue behavior of AM topologically ordered biodegradable porous iron both in r-SBF and in air. The parallel design of the study allowed us to unravel two novel aspects of this category of AM biomaterials: (i) the effect of material type on fatigue behavior and (ii) the mutual influences of biodegradation and cyclic loading. Interestingly, while biodegradation only slightly decreased the fatigue strength of porous iron from $0.7\sigma_y$ in air to $0.65\sigma_y$ in r-SBF, cyclic loading significantly increased its biodegradation rate, particularly at higher stress levels. This is very different from AM porous magnesium [18] both quantitatively and qualitatively. Quantitatively speaking, the fatigue strength of AM porous iron is about 2-3 times higher than that of AM porous magnesium both in air and in r-SBF. In qualitative terms, the effect of biodegradation on the fatigue life of the porous WE43 magnesium alloy was much stronger than that of porous iron. The effect of cyclic loading on the biodegradation rates of porous iron and WE43 magnesium was, however, quite significant and in that sense were not quite different. While some of these differences (*e.g.*, the effect of biodegradation on fatigue life) can be easily explained by

the faster biodegradation of WE43 [14], explaining other observations (*e.g.*, higher fatigue strength in air) requires a more in-depth analysis. For one thing, the intrinsic mechanical properties of the material itself must be the main reason that pure iron is much more ductile than the WE43 magnesium alloy. For another, printing quality, e.g., the difference in surface morphology and defects, such as internal pores, can affect the fatigue performance of all AM metallic scaffolds to different extents [23].

Further morphological and microstructural examinations of fatigue-tested porous iron showed that fatigue cracks preferably initiated at the strut junctions of the specimens tested both in air and in r-SBF. In r-SBF, localized degradation accelerated by cyclic loading may have promoted crack initiation. A higher degradation rate at a higher stress level could be contributed by higher internal stresses, according to EBSD and XRD analysis. Unlike titanium scaffolds [24], crack tips in the iron scaffolds were found to be blunt instead of being sharp, because of the good ductility of the latter. The cycle number that an implant needs to sustain in the first months after surgery is typically between 0.1×10^6 and 1×10^6 cycles [25]. The average patient's walking activity is around 2×10^6 cycles per year [3]. In this study, the SLM iron scaffolds did not fail at $0.65\sigma_y$ up to 3×10^6 cycles in r-SBF, making it qualified as a highly fatigue-resistant biodegradable porous biomaterial.

4.1. Effect of microstructure on biodegradation and fatigue behavior

Microstructure can influence both the biodegradation behavior and fatigue behavior of a material. SLM iron was found to have a higher degradation rate than the cold-rolled counterpart [15], as SLM led to the formation of fine grains. Generally, as SLM involves rapid solidification and high cooling rates, resulting grain sizes are usually much finer than those of conventionally manufactured counterparts. According to the classical solidification theory, grain morphology is determined by the ratio of thermal gradient, G, and solidification rate velocity, R [26]. On the top of the melt pool, the grains are more likely to be fine and

equiaxed, because of low G/R ratios [27, 28]. At the bottom of the melt pool, however, the thermal gradient is greater than that on the top and heterogeneous nucleation may be induced when the previous layer is re-melted. Columnar grains may thus be formed at the bottom [29]. Moreover, unlike previously reported AM solid iron [30, 31], the AM porous scaffolds had only a limited number of elongated grains oriented in parallel with the length of the strut. This indicates that the effect of directional solidification would not be as strong as in the case of the solid counterpart. As the struts of the iron scaffolds were built in a tilted direction, the scanning contours were offset layer by layer, which could be the reason why some grains were elongated along the length of struts. Columnar grain growth may be restrained by the formation of equiaxed grains on the surface of the melt pool. When the re-melted depth is smaller than the equiaxed grains [32], a mixture of fine equiaxed grains and columnar grains will be formed. Furthermore, the microstructure of SLM porous iron being different from that of solid parts can also be caused by different thermal boundary conditions, as the melt pool is surrounded much more by a powder bed (with low thermal conductivity) when scanning a strut. Small grains increase the area of grain boundaries that are more reactive in the corrosive medium [33-35]. In fact, the increased biodegradation is beneficial, given the fact that the biodegradation rate of iron is normally considered to be too low [36, 37]. In terms of the fatigue behavior, fine grains are usually capable of inhibiting crack initiation and increasing the number of barriers to early crack propagation [38]. Moreover, the good ductility of pure iron itself can improve the fatigue properties of AM iron scaffolds. As the stress concentration factor, K_t, and fatigue notch factor, K_f, are both important for the fatigue behavior, the notch sensitivity q, *i.e.* $(1- K_f)/(1- K_t)$, is frequently used to express the degree of difference between these two quantities. K_f is dependent not only on the specimen geometry but also on the material properties [39]. For a material with good ductility, as the plastic deformation in the vicinity of crack tips reduces the influence of stress concentration

on crack growth, K_t is normally lower than K_f [40, 41]. The notch sensitivity, q, is therefore lower for ductile materials than brittle ones [41]. The failure mode of the iron scaffolds is different from that of the AM porous titanium reported in the literature [2]. There was no fracture plane through the iron scaffolds (Fig. 3c) and the cracks were blunting (Fig. 5c, Fig. 6c) instead of propagating sharply through the whole strut. As discussed above, this could be attributed to the high ductility of iron.

In addition, defects, such as pores caused by lack of fusion, may affect the fatigue behavior of AM iron as well. Internal pores and unmelted powder particles on the strut surface could both serve as stress concentration sites for fatigue crack initiation [2]. As the internal pore volume fraction was found to be negligibly low in the present AM iron scaffolds, it would be beneficial for their fatigue resistance.

4.2. Effect of cyclic loading on biodegradation

The corrosion products formed on the surface of scaffold struts could fall off under cyclic loading, as their mechanical properties are totally different from those of the iron substrate. Furthermore, the extrusion and intrusion of persistent slip bands during cyclic loading may break up the layer of corrosion products at the surface [17]. In addition, pitting potentials under cyclic loading are much smaller than those without stress, and the pitting potentials decrease with increasing stress level [42-45]. The acceleration of pitting degradation may promote intergranular degradation [42]. For topologically ordered porous structures, stress distribution follows a certain pattern. Taking the diamond unit cell lattice structure as an example, tensile stress tends to be concentrated at the strut junctions according to the results obtained from FE modeling (Fig. 6j). Concentrated tensile stress can cause micro residual stress and local strain, which can be seen in the KAM maps (Fig. 7c and d) and FWHM (Fig. 8b). KAM quantifies the average misorientation around a measurement point with respect to a defined set of nearest neighbor points [46]. It therefore provides a qualitative measurement

of the distribution of micro residual stresses or local strains [47]. Local strains cause dislocations to slip and multiply in iron grains. Because of the barrier effect of grain boundaries, the slipped dislocations pile-up at these interfaces and normally this phenomenon is more obvious at higher cyclic stress levels [42]. FWHM is related to the dislocation density and the so-called type II micro residual stresses [48]. For the specimens tested under the loading stress level of $0.9\sigma_y$, there were more obvious local strain concentrations around the cracks (Fig. 7c), leading to larger FWHM values (Fig. 8b) than those tested at $0.65\sigma_y$. However, as the curvature of AM porous materials does not allow for accurate FWHM readings, the increase of FWHM values is not obvious. The slip bands and dislocation pile-ups at the strut junctions are the preferred sites for cracks to initiate because of stress concentration [49]. Consequently, cyclic loading increased the degradation rate of the specimens in r-SBF. This increase was substantial at higher stress levels (Fig. 3d). The increased biodegradation rate was confirmed by the analysis of ion concentrations (Ca, P) in r-SBF (Fig. 3e and f). The faster biodegradation rate may favor the formation of corrosion products. The rise of pH value may facilitate the precipitation and deposition of phosphates, including $Mg_3(PO_4)_2$, $Ca_{10}(PO_4)_6(OH)_2$, and $Fe_3(PO_4)_2{\cdot}8H_2O$ [50]. Indeed, for the specimens in r-SBF under cyclic loading, the concentrations of Ca and P ions were lower in r-SBF, while more Ca and P contents were found in the corrosion products (Fig. 4).

4.3. Effect of biodegradation on fatigue properties

In addition to crack initiation and propagation, strain accumulation can affect the fatigue properties of a porous metallic structure [24, 51]. At the early stages of fatigue testing, the fatigue behavior of the iron scaffolds is controlled by strain ratcheting, which may be caused by the cyclic strain ratcheting of the unit cell [52, 53]. Higher stresses leads to higher ratcheting strain rates of the unit cells. As cyclic loading progresses, the cyclic softening of porous metallic structure starts to contribute to crack initiation and propagation as well [24,

51, 54]. In this study, the strain ratcheting rates of the iron scaffolds in air and in r-SBF were quite similar (Fig. 3a), probably because the overall amount of biodegradation was quite small. For example, under cyclic loading at $0.9\sigma_y$, only 0.07±0.03 mg iron was lost from the specimen after fatigue testing (Fig. 3d). Such a slight mass loss would not substantially weaken the entire scaffold. However, according to the S-N curve, at the same stress levels, the fatigue strengths of the Fe scaffolds all decreased from those in air to those in r-SBF (Fig. 3b). The localized biodegradation occurring to the specimens in r-SBF could be the main reason behind this, as the pits created could act as the preferred sites for crack initiation (Fig. 6f and i) [55]. Furthermore, biodegradation could accelerate fatigue crack propagation, as anodic reaction or hydrogen embrittlement might occur at the crack tips [56].

In r-SBF, the above-mentioned slip bands and dislocation pile-ups (section 4.2) could increase the chemical and electrochemical potentials [42, 57]. Iron ion dissolution at or near dislocations and slip bands may form pits, which will in turn introduce higher stress concentrations [56]. Crack may then initiate as soon as the local stress concentration reaches a certain value. In addition, it has been reported that iron oxide could be easily formed on fresh slip bands due to its high chemical activity [56]. Subsequently, if the previously extruded slip bands intrude back, some hard iron oxides may be carried into the surface of the specimen. The corrosion products can impede the normal slipping of slip bands and, thus, may initiate cracks. At a high stress level, the mechanical damage may play a more important role than the corrosion attack in crack initial propagation [47]. This may be the reason why at $0.9\sigma_y$, crack initiation did not show clear differences between the specimens in r-SBF and in air, while at $0.65\sigma_y$, there were more cracks initiated at the strut junctions in the iron scaffolds tested in r-SBF, as compared to the specimens tested in air (Fig. 5e, f).

5. Conclusions

The AM porous iron exhibited extraordinarily high fatigue resistance, even when fatigue was accompanied and influenced by biodegradation in r-SBF. Indeed, biodegradation only reduced the fatigue strength of the SLM iron scaffolds from $0.7\sigma_y$ in air to $0.65\sigma_y$ in r-SBF. On the other hand, cyclic loading significantly accelerated the biodegradation rate, especially at higher stress levels. Cracks preferred to initiate at the strut junctions where tensile stresses were concentrated. Cyclic loading introduced micro strain-favored pit formation, which in turn promoted crack initiation. The extraordinarily high fatigue resistance and slow degradation rate make AM porous iron a promising biodegradable metallic material for bone substitution.

DATA AVAILABILITY

The raw/processed data required to reproduce these findings cannot be shared at this time as the data also forms part of an ongoing study.

ACKNOWLEDGEMENTS

The research was financially supported by the Prosperos project, funded by the Interreg VA Flanders – The Netherlands program, CCI Grant No. 2014TC16RFCB04. Funding from the START-Program (Grant No. 691513/696601) of the Faculty of Medicine, RWTH Aachen University to H.J. is also acknowledged. K.L. thanks VLAIO (Flanders Agency for Innovation and Entrepreneurship) for the financial support (IWT140257). Mr. R.M. Huizenga at the Department of Materials Science and Engineering of the Delft University of Technology is acknowledged for the XRD analysis. Y.L. also thanks the China Scholarship Council (CSC) for financial support.

REFERENCES

[1] C. Yan, L. Hao, A. Hussein, P. Young, D. Raymont. Advanced lightweight 316L stainless steel cellular lattice structures fabricated via selective laser melting. Mater Des. 2014;55:533-541.

[2] S. M. Ahmadi, R. Hedayati, Y. Li, K. Lietaert, N. Tümer, A. Fatemi, C. D. Rans, B. Pouran, H. Weinans, A. A. Zadpoor. Fatigue performance of additively manufactured meta-biomaterials: The effects of topology and material type. Acta Biomater. 2018;65:292-304.

[3] F. Bobbert, K. Lietaert, A. Eftekhari, B. Pouran, S. Ahmadi, H. Weinans, A. Zadpoor. Additively manufactured metallic porous biomaterials based on minimal surfaces: A unique combination of topological, mechanical, and mass transport properties. Acta Biomater. 2017;53:572-584.
[4] R. Hedayati, S. M. Ahmadi, K. Lietaert, B. Pouran, Y. Li, H. Weinans, C. D. Rans, A. A. Zadpoor. Isolated and modulated effects of topology and material type on the mechanical properties of additively manufactured porous biomaterials. J Mech Behav Biomed Mater. 2018;79:254-263.
[5] J. van der Stok, M. K. E. Koolen, M. de Maat, S. Amin Yavari, J. Alblas, P. Patka, J. Verhaar, E. van Lieshout, A. A. Zadpoor, H. Weinans, H. Jahr. Full regeneration of segmental bone defects using porous titanium implants loaded with BMP-2 containing fibrin gels. Eur Cell Mater. 2015;2015:141-154.
[6] A. Zadpoor. Frontiers of Additively Manufactured Metallic Materials. Materials. 2018;11:1566.
[7] F. Bobbert, A. Zadpoor. Effects of bone substitute architecture and surface properties on cell response, angiogenesis, and structure of new bone. J Mater Chem B. 2017.
[8] Y. F. Zheng, X. N. Gu, F. Witte. Biodegradable metals. Mater Sci Eng R Rep. 2014;77:1-34.
[9] M. Moravej, D. Mantovani. Biodegradable Metals for Cardiovascular Stent Application: Interests and New Opportunities. Int J Mol Sci. 2011;12:4250.
[10] Z. Wen, L. Zhang, C. Chen, Y. Liu, C. Wu, C. Dai. A construction of novel iron-foam-based calcium phosphate/chitosan coating biodegradable scaffold material. Materials Science and Engineering: C. 2013;33:1022-1031.
[11] D.-T. Chou, D. Wells, D. Hong, B. Lee, H. Kuhn, P. N. Kumta. Novel processing of iron–manganese alloy-based biomaterials by inkjet 3-D printing. Acta Biomater. 2013;9:8593-8603.
[12] D. Hong, D.-T. Chou, O. I. Velikokhatnyi, A. Roy, B. Lee, I. Swink, I. Issaev, H. A. Kuhn, P. N. Kumta. Binder-jetting 3D printing and alloy development of new biodegradable Fe-Mn-Ca/Mg alloys. Acta Biomater. 2016;45:375-386.
[13] C. Yang, Z. Huan, X. Wang, C. Wu, J. Chang. 3D Printed Fe Scaffolds with HA Nanocoating for Bone Regeneration. ACS Biomater Sci Eng. 2018;4:608-616.
[14] Y. Li, J. Zhou, P. Pavanram, M. A. Leeflang, L. I. Fockaert, B. Pouran, N. Tümer, K. U. Schröder, J. M. C. Mol, H. Weinans, H. Jahr, A. A. Zadpoor. Additively manufactured biodegradable porous magnesium. Acta Biomater. 2018;67:378-392.
[15] Y. Li, H. Jahr, K. Lietaert, P. Pavanram, A. Yilmaz, L. I. Fockaert, M. A. Leeflang, B. Pouran, Y. Gonzalez-Garcia, H. Weinans, J. M. C. Mol, J. Zhou, A. A. Zadpoor. Additively manufactured biodegradable porous iron. Acta Biomater. 2018;77:380-393.
[16] A. P. Md Saad, A. Syahrom. Study of dynamic degradation behaviour of porous magnesium under physiological environment of human cancellous bone. Corros Sci. 2018;131:45-56.
[17] X. N. Gu, W. R. Zhou, Y. F. Zheng, Y. Cheng, S. C. Wei, S. P. Zhong, T. F. Xi, L. J. Chen. Corrosion fatigue behaviors of two biomedical Mg alloys – AZ91D and WE43 – In simulated body fluid. Acta Biomater. 2010;6:4605-4613.
[18] Y. Li, H. Jahr, X.-Y. Zhang, M. A. Leeflang, W. Li, B. Pouran, F. D. Tichelaar, H. Weinans, J. Zhou, A. A. Zadpoor. Biodegradation-affected fatigue behavior of additively manufactured porous magnesium.submitted.
[19] S. M. Ahmadi, R. Hedayati, Y. Li, K. Lietaert, N. Tümer, A. Fatemi, C. D. Rans, B. Pouran, H. Weinans, A. A. Zadpoor. Fatigue performance of additively manufactured meta-biomaterials: The effects of topology and material type. Acta Biomater. 2017.
[20] A. Oyane, H.-M. Kim, T. Furuya, T. Kokubo, T. Miyazaki, T. Nakamura. Preparation and assessment of revised simulated body fluids. J Biomed Mater Res A. 2003;65A:188-195.
[21] A. P. Md. Saad, N. Jasmawati, M. N. Harun, M. R. Abdul Kadir, H. Nur, H. Hermawan, A. Syahrom. Dynamic degradation of porous magnesium under a simulated environment of human cancellous bone. Corros Sci. 2016;112:495-506.
[22] Y. C. Lin, Z.-H. Liu, X.-M. Chen, J. Chen. Uniaxial ratcheting and fatigue failure behaviors of hot-rolled AZ31B magnesium alloy under asymmetrical cyclic stress-controlled loadings. Materials Science and Engineering: A. 2013;573:234-244.

[23] S. M. Ahmadi, R. Kumar, E. V. Borisov, R. Petrov, S. Leeflang, Y. Li, N. Tümer, R. Huizenga, C. Ayas, A. A. Zadpoor, V. A. Popovich. From microstructural design to surface engineering: A tailored approach for improving fatigue life of additively manufactured meta-biomaterials. Acta Biomater. 2019;83:153-166.
[24] S. J. Li, L. E. Murr, X. Y. Cheng, Z. B. Zhang, Y. L. Hao, R. Yang, F. Medina, R. B. Wicker. Compression fatigue behavior of Ti–6Al–4V mesh arrays fabricated by electron beam melting. Acta Mater. 2012;60:793-802.
[25] R. Hedayati, S. M. Ahmadi, K. Lietaert, N. Tümer, Y. Li, S. Amin Yavari, A. A. Zadpoor. Fatigue and quasi-static mechanical behavior of bio-degradable porous biomaterials based on magnesium alloys. J Biomed Mater Res A. 2018;106:1798-1811.
[26] J. Dupont. Fundamentals of Weld Solidification. ASM Handbook.6:700.
[27] F. Yan, W. Xiong, E. Faierson. Grain Structure Control of Additively Manufactured Metallic Materials. Materials. 2017;10:1260.
[28] Y. Zhu, D. Liu, X. Tian, H. Tang, H. Wang. Characterization of microstructure and mechanical properties of laser melting deposited Ti–6.5Al–3.5Mo–1.5Zr–0.3Si titanium alloy. Mater Des. 2014;56:445-453.
[29] V. Manakari, G. Parande, M. Gupta. Selective Laser Melting of Magnesium and Magnesium Alloy Powders: A Review. Metals. 2016;7:2.
[30] A. Simchi, H. Pohl. Effects of laser sintering processing parameters on the microstructure and densification of iron powder. Mater Sci Eng, A. 2003;359:119-128.
[31] B. Song, S. Dong, Q. Liu, H. Liao, C. Coddet. Vacuum heat treatment of iron parts produced by selective laser melting: Microstructure, residual stress and tensile behavior. Mater Des. 2014;54:727-733.
[32] T. Wang, Y. Y. Zhu, S. Q. Zhang, H. B. Tang, H. M. Wang. Grain morphology evolution behavior of titanium alloy components during laser melting deposition additive manufacturing. J Alloys Compd. 2015;632:505-513.
[33] C. S. Obayi, R. Tolouei, A. Mostavan, C. Paternoster, S. Turgeon, B. A. Okorie, D. O. Obikwelu, D. Mantovani. Effect of grain sizes on mechanical properties and biodegradation behavior of pure iron for cardiovascular stent application. Biomatter. 2016;6:e959874.
[34] M. Moravej, S. Amira, F. Prima, A. Rahem, M. Fiset, D. Mantovani. Effect of electrodeposition current density on the microstructure and the degradation of electroformed iron for degradable stents. Mater Sci Eng, B. 2011;176:1812-1822.
[35] P. K. Rai, S. Shekhar, K. Mondal. Development of gradient microstructure in mild steel and grain size dependence of its electrochemical response. Corros Sci. 2018;138:85-95.
[36] T. Kraus, F. Moszner, S. Fischerauer, M. Fiedler, E. Martinelli, J. Eichler, F. Witte, E. Willbold, M. Schinhammer, M. Meischel, P. J. Uggowitzer, J. F. Löffler, A. Weinberg. Biodegradable Fe-based alloys for use in osteosynthesis: Outcome of an in vivo study after 52weeks. Acta Biomater. 2014;10:3346-3353.
[37] M. Peuster, C. Hesse, T. Schloo, C. Fink, P. Beerbaum, C. von Schnakenburg. Long-term biocompatibility of a corrodible peripheral iron stent in the porcine descending aorta. Biomaterials. 2006;27:4955-4962.
[38] Z. Zúberová, L. Kunz, T. T. Lamark, Y. Estrin, M. Janeček. Fatigue and Tensile Behavior of Cast, Hot-Rolled, and Severely Plastically Deformed AZ31 Magnesium Alloy. Metall Mater Trans A. 2007;38:1934-1940.
[39] G. K. Haritos, T. Nicholas, D. B. Lanning. Notch size effects in HCF behavior of Ti–6Al–4V. Int J Fatigue. 1999;21:643-652.
[40] A. M. Sherman, R. G. Davies. The effect of martensite content on the fatigue of a dual-phase steel. Int J Fatigue. 1981;3:36-40.
[41] Z.-Z. Hu, S.-Z. Cao. Relationship between fatigue notch factor and strength. Eng Fract Mech. 1994;48:127-136.

[42] J. Xie, A. T. Alpas, D. O. Northwood. A mechanism for the crack initiation of corrosion fatigue of Type 316L stainless steel in Hank's solution. Mater Charact. 2002;48:271-277.
[43] J. Yang, Q. Wang, K. Guan. Effect of stress and strain on corrosion resistance of duplex stainless steel. Int J Pressure Vessels Piping. 2013;110:72-76.
[44] G. LÜ, H. Cheng, C. Xu, Z. He. Effect of Strain and Chloride Concentration on Pitting Susceptibility for Type 304 Austenitic Stainless Steel*. Chin J Chem Eng. 2008;16:314-319.
[45] B. T. Lu, Z. K. Chen, J. L. Luo, B. M. Patchett, Z. H. Xu. Pitting and stress corrosion cracking behavior in welded austenitic stainless steel. Electrochimica Acta. 2005;50:1391-1403.
[46] S. I. Wright, M. M. Nowell, D. P. Field. A Review of Strain Analysis Using Electron Backscatter Diffraction. Microsc Microanal. 2011;17:316-329.
[47] T. Zhao, Z. Liu, C. Du, C. Dai, X. Li, B. Zhang. Corrosion fatigue crack initiation and initial propagation mechanism of E690 steel in simulated seawater. Mater Sci Eng, A. 2017;708:181-192.
[48] I. Fernández Pariente, M. Guagliano. About the role of residual stresses and surface work hardening on fatigue ΔKth of a nitrided and shot peened low-alloy steel. Surf Coat Technol. 2008;202:3072-3080.
[49] D. Bian, W. Zhou, Y. Liu, N. Li, Y. Zheng, Z. Sun. Fatigue behaviors of HP-Mg, Mg–Ca and Mg–Zn–Ca biodegradable metals in air and simulated body fluid. Acta Biomater. 2016;41:351-360.
[50] R. Gorejová, L. Haverová, R. Oriňaková, A. Oriňak, M. Oriňak. Recent advancements in Fe-based biodegradable materials for bone repair. Journal of Materials Science. 2018.
[51] Y. J. Liu, H. L. Wang, S. J. Li, S. G. Wang, W. J. Wang, W. T. Hou, Y. L. Hao, R. Yang, L. C. Zhang. Compressive and fatigue behavior of beta-type titanium porous structures fabricated by electron beam melting. Acta Mater. 2017;126:58-66.
[52] A. M. Harte, N. A. Fleck, M. F. Ashby. Fatigue failure of an open cell and a closed cell aluminium alloy foam. Acta Mater. 1999;47:2511-2524.
[53] McCullough, Fleck. The stress–life fatigue behaviour of aluminium alloy foams. Fatigue Fract Eng Mater Struct. 2000;23:199-208.
[54] J. Zhou, W. O. Soboyejo. Compression–compression fatigue of open cell aluminum foams: macro-/micro- mechanisms and the effects of heat treatment. Mater Sci Eng, A. 2004;369:23-35.
[55] L. Chen, Y. Sheng, H. Zhou, Z. Li, X. Wang, W. Li. Influence of a MAO + PLGA coating on biocorrosion and stress corrosion cracking behavior of a magnesium alloy in a physiological environment. Corros Sci. 2019;148:134-143.
[56] W. Zhao, Y. Wang, T. Zhang, Y. Wang. Study on the mechanism of high-cycle corrosion fatigue crack initiation in X80 steel. Corros Sci. 2012;57:99-103.
[57] Y. Zheng, Y. Li, J. Chen, Z. Zou. Effects of tensile and compressive deformation on corrosion behaviour of a Mg–Zn alloy. Corros Sci. 2015;90:445-450.

Figure captions:

Figure 1. Iron scaffold design and corrosion fatigue test setup: (a) diamond unit cell; (b) scaffold; (c) corrosion fatigue test setup. BD: building direction.

Figure 2. EBSD characterization of AM iron scaffold struts on the longitudinal section: (a) IQ map; (b) IPF map; (c) PF. BD: building direction; SLD: strut length direction.

Figure 3. Fatigue behavior of the AM iron scaffold specimens in air and in r-SBF: (a) ratcheting rate; (b) S-N curve; (c) failure mode; (d) degradation rate; (e) Ca and (f) P ion concentrations.

Figure 4. Corrosion products analysis: (a) (b) surface morphology of as-built specimen; (c) (d) specimens after static immersion in r-SBF (c) and after fatigue test in r-SBF under $0.9\sigma_y$ dynamic loading (d); (e) (f) specimens after static immersion in r-SBF (e) and after fatigue test under $0.75\sigma_y$ dynamic loading (f); (g) (h) specimens after static immersion in r-SBF (g) and after fatigue test under $0.65\sigma_y$ dynamic loading (h). Arrow: EDS analysis points; red square: localized degradation and higher magnification overlay; scale bar: (a) 500 μm; (b-h) 50 μm.

Figure 5. Fatigue crack distributions in the whole scaffold: (a) (b) specimens after fatigue test till 2% strain in air (a) and in r-SBF at $0.9\sigma_y$ (b); (c) (d) specimens after fatigue test till 5% strain in air (c) and in r-SBF at $0.9\sigma_y$ (d); (e) (f) specimens after 3×10^6 cycles of fatigue test at $0.65\sigma_y$ in air (e) and in r-SBF (f). Circles: cracks; area between two parallel lines: deformed struts; scale bar: 200 μm.

Figure 6. Fatigue crack morphologies: (a) (b) (c) specimen after fatigue test until 5% strain in air at $0.9\sigma_y$; (d) (e) (f) specimen after fatigue test until 5% strain in r-SBF at $0.9\sigma_y$; (g) (h) (i) specimen after 3×10^6 cycles of fatigue test in r-SBF at $0.65\sigma_y$; (j) stress distribution in a diamond unit cell under compressive loading. Circles: cracks; square: pitting.

Figure 7. EBSD characterization of the fatigue crack track in air: (a) IQ map of the specimen tested at $0.9\sigma_y$; (b) IPF map of the specimen tested at $0.9\sigma_y$; (c) KAM map of the specimen tested at $0.9\sigma_y$; (d) KAM map of the specimen tested at $0.65\sigma_y$; (e) KAM map of the as-built sample.

Figure 8. XRD analysis of the AM porous iron before and after the fatigue test in air at $0.9\sigma_y$: (a) XRD patterns; (b) FWHM.

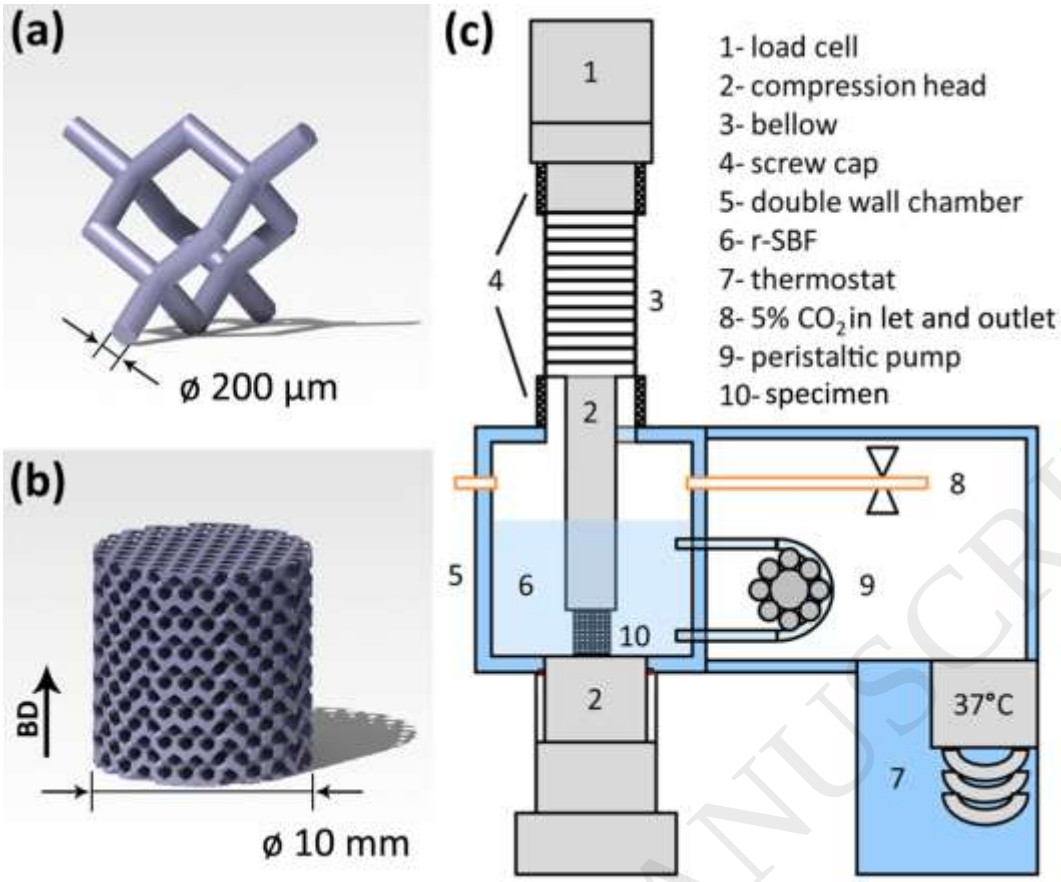

Figure 1. Iron scaffold design and corrosion fatigue test setup: (a) diamond unit cell; (b) scaffold; (c) corrosion fatigue test setup. BD: building direction.

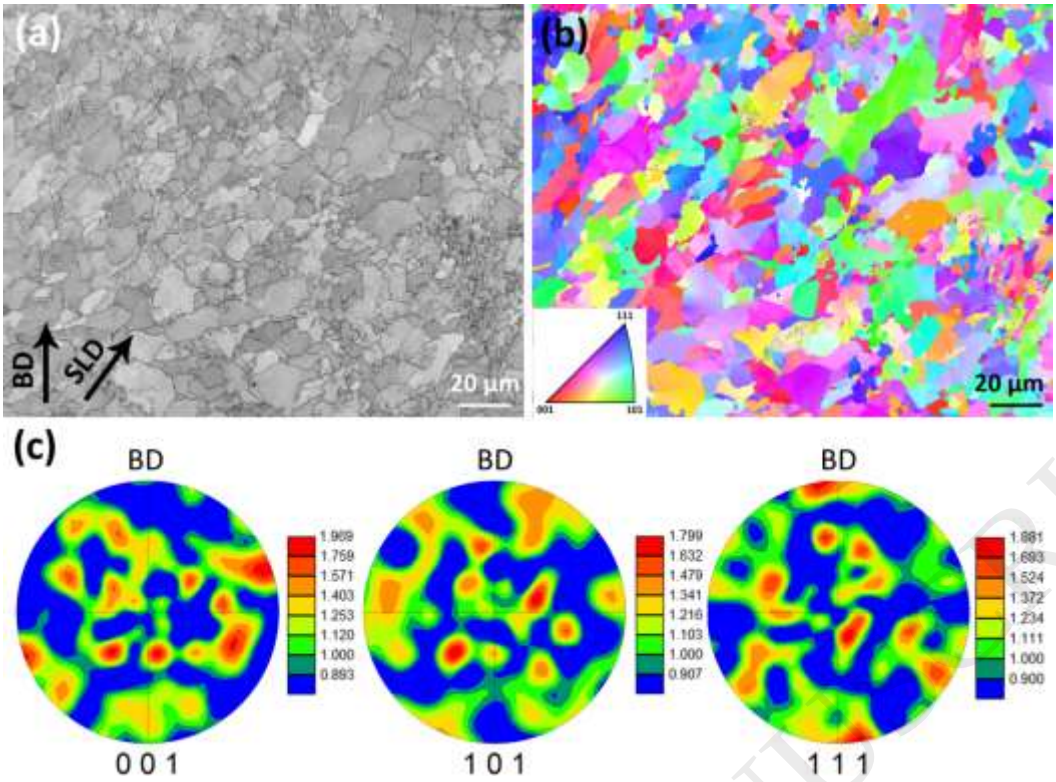

Figure 2. EBSD characterization of AM iron scaffold struts on the longitudinal section: (a) IQ map; (b) IPF map; (c) PF. BD: building direction; SLD: strut length direction.

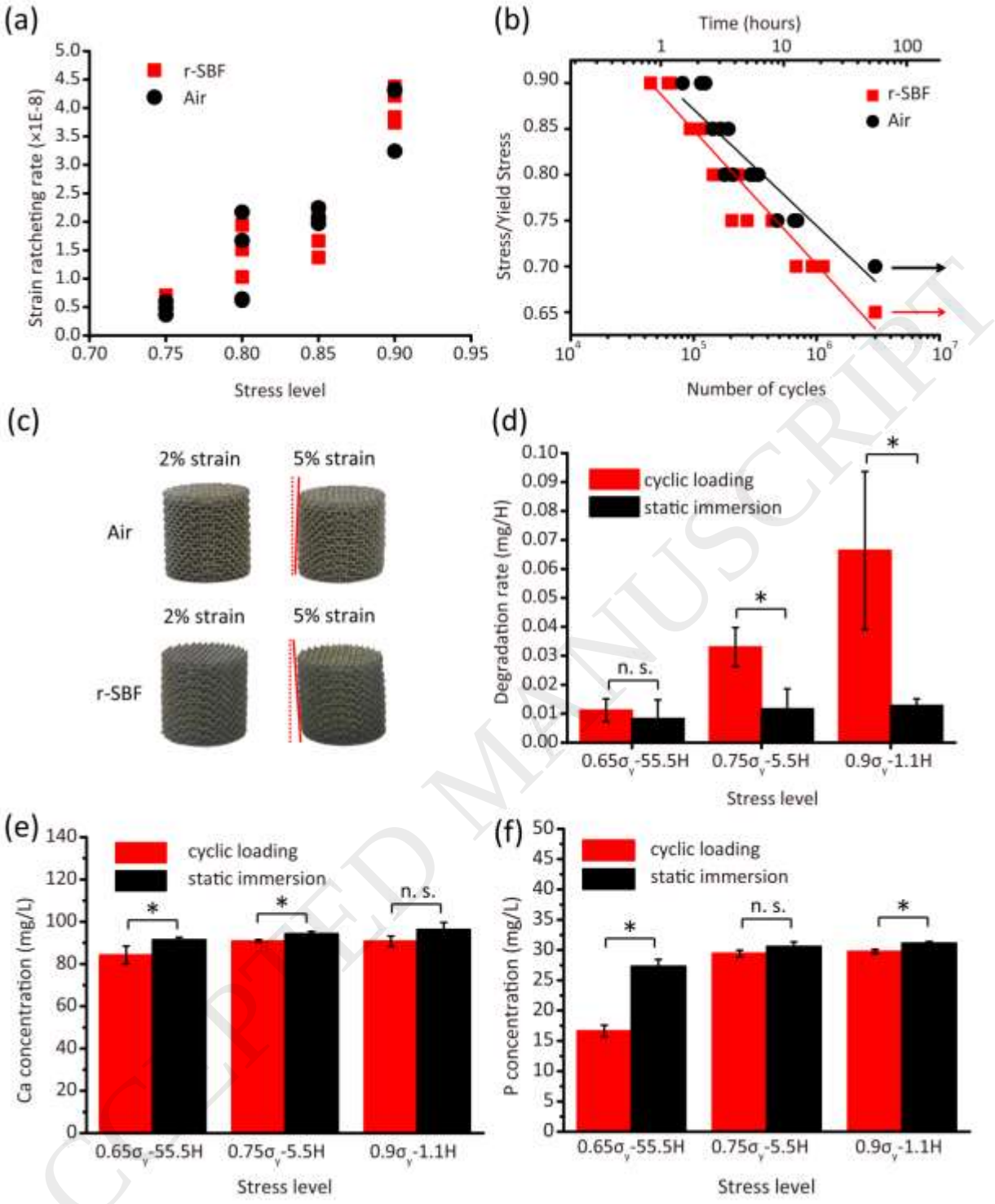

Figure 3. Fatigue behavior of the AM iron scaffold specimens in air and in r-SBF: (a) ratcheting rate; (b) S-N curve; (c) failure mode; (d) degradation rate; (e) Ca and (f) P ion concentrations.

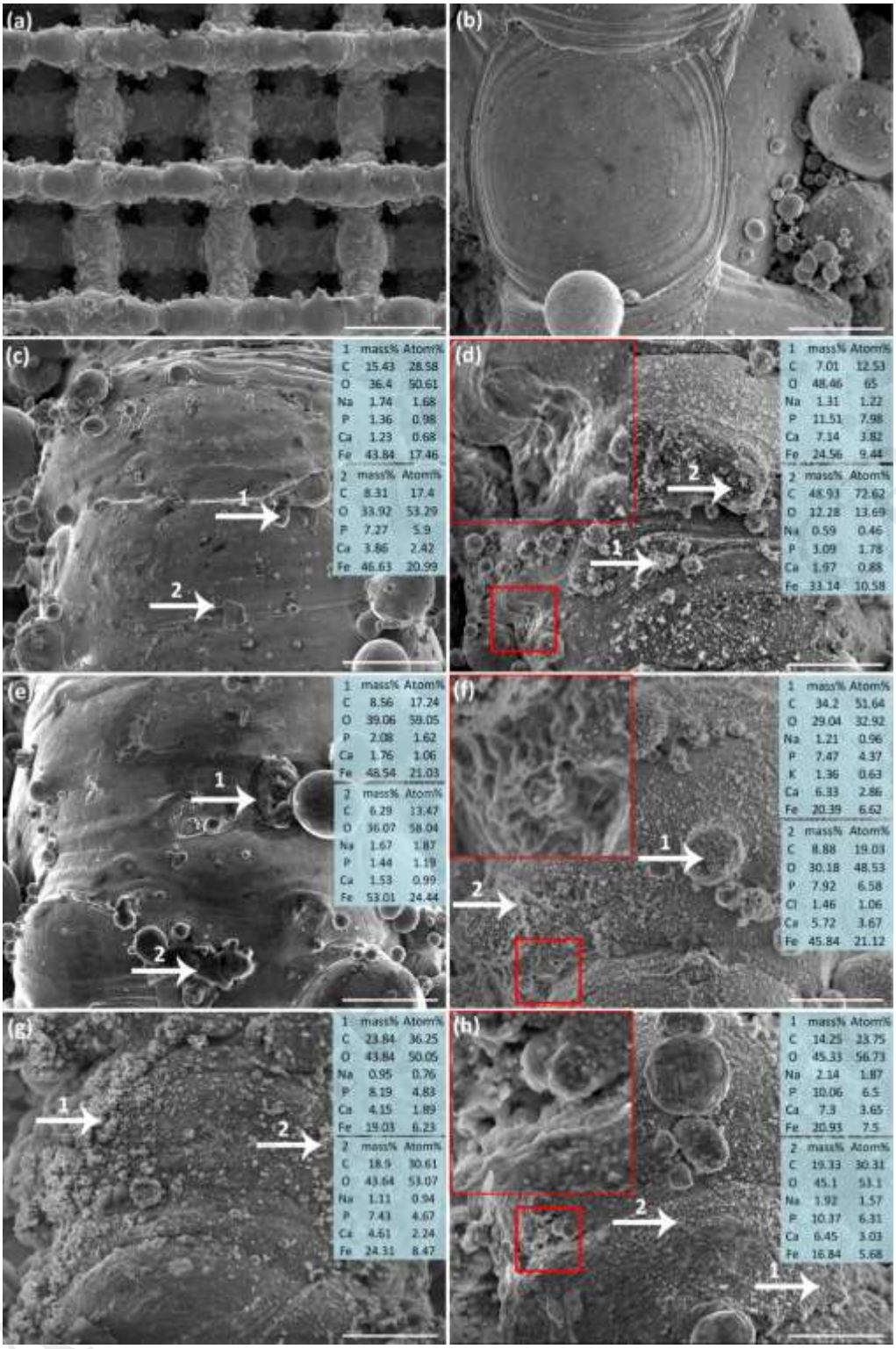

Figure 4. Corrosion products analysis: (a) (b) surface morphology of the as-built specimen; (c) (d) specimens after static immersion in r-SBF (c) and after fatigue test in r-SBF under $0.9\sigma_y$ dynamic loading (d); (e) (f) specimens after static immersion in r-SBF (e) and after fatigue test under $0.75\sigma_y$ dynamic loading (f); (g) (h) specimens after static immersion in r-SBF (g) and after fatigue test under $0.65\sigma_y$ dynamic loading (h). Arrow: EDS analysis points; red square: localized degradation and higher magnification overlay; scale bar: (a) 500 μm; (b-h) 50 μm.

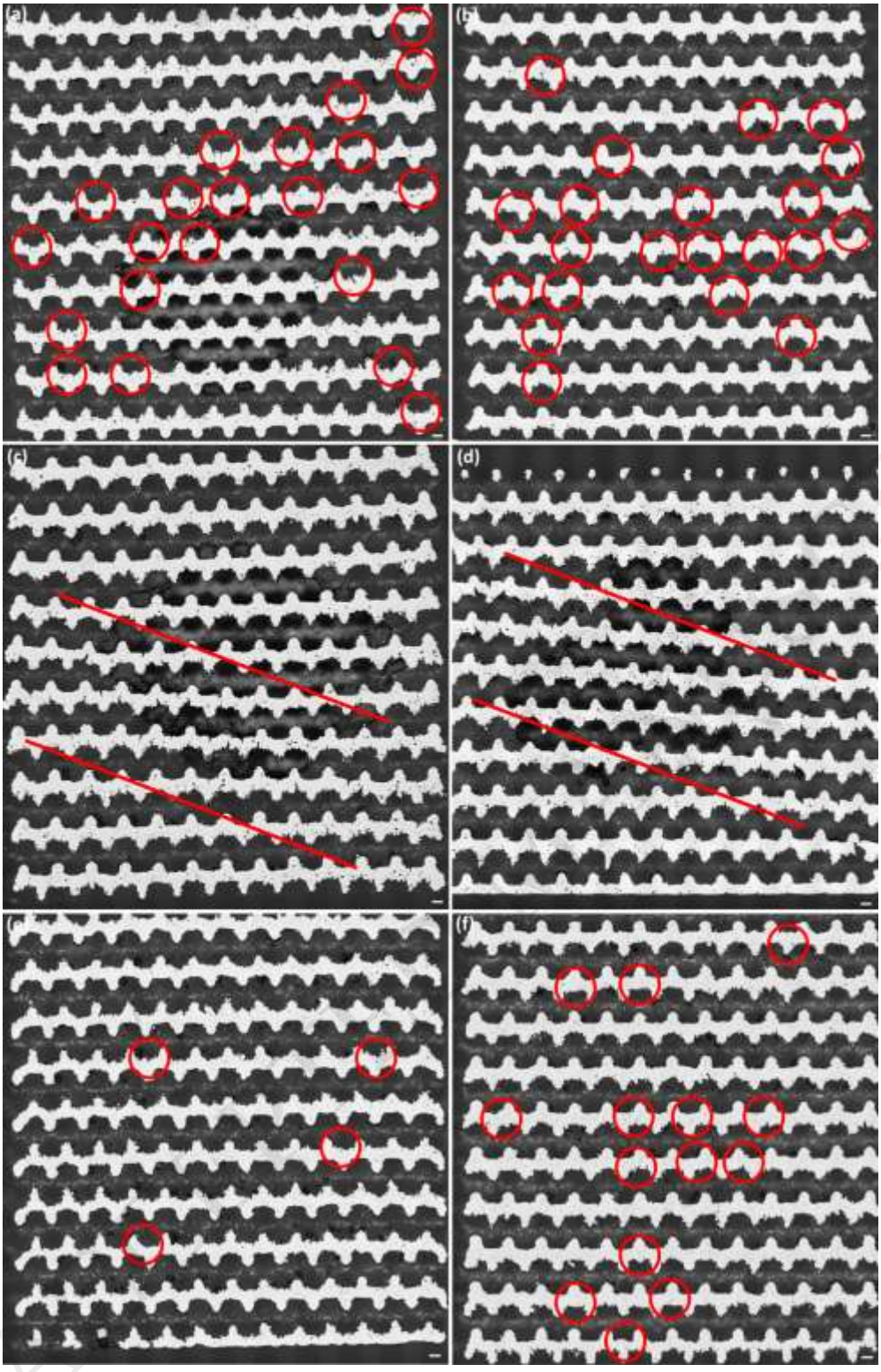

Figure 5. Fatigue crack distributions in the whole scaffold: (a) (b) specimens after fatigue test till 2% strain in air (a) and in r-SBF at $0.9\sigma_y$ (b); (c) (d) specimens after fatigue test till 5% strain in air (c) and in r-SBF at $0.9\sigma_y$ (d); (e) (f) specimens after 3×10^6 cycles of fatigue test at $0.65\sigma_y$ in air (e) and in r-SBF (f). Circles: cracks; area between two parallel lines: deformed struts; scale bar: 200 μm.

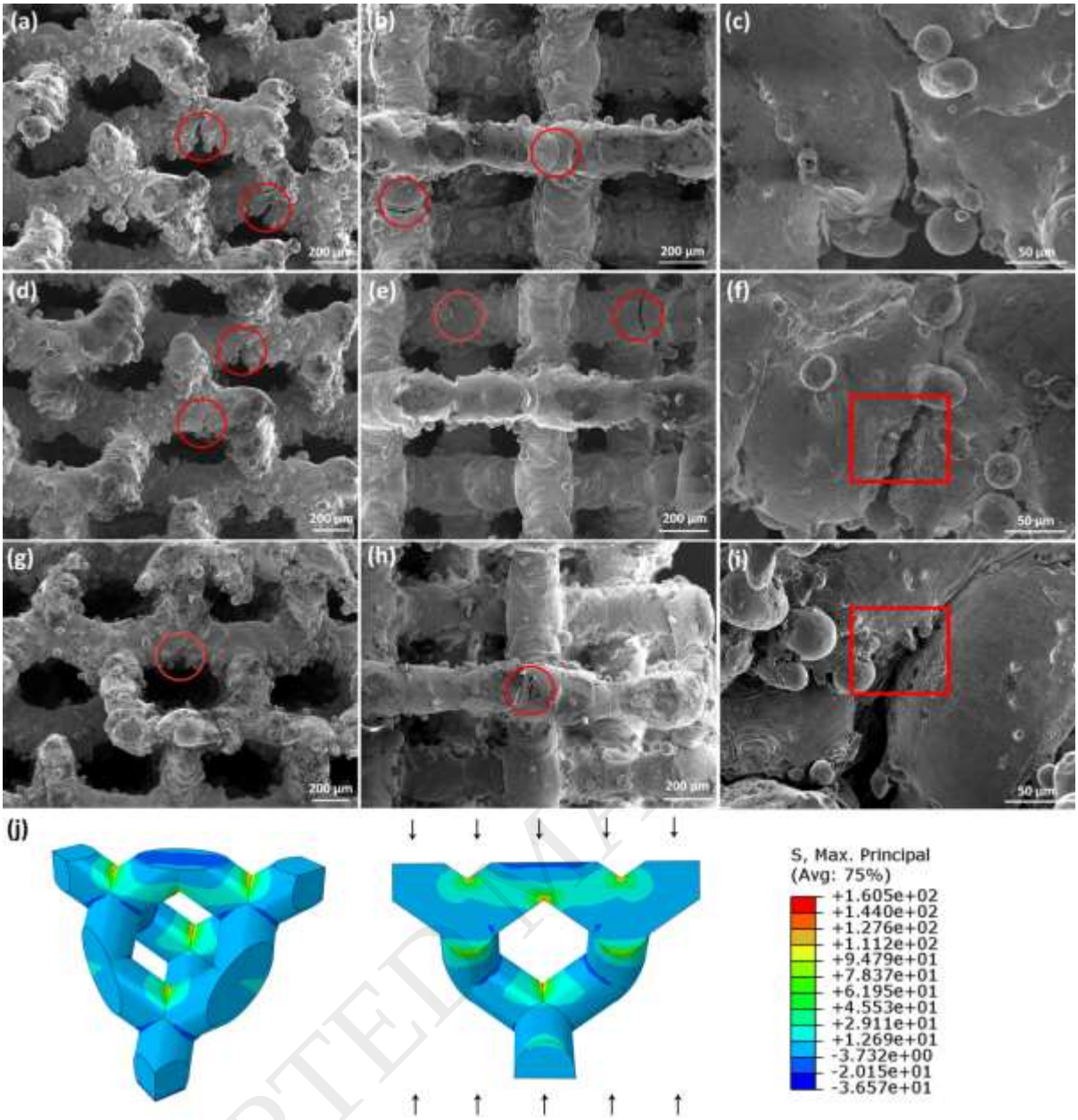

Figure 6. Fatigue crack morphologies: (a) (b) (c) specimen after fatigue test until 5% strain in air at $0.9\sigma_y$; (d) (e) (f) specimen after fatigue test until 5% strain in r-SBF at $0.9\sigma_y$; (g) (h) (i) specimen after 3×10^6 cycles of fatigue test in r-SBF at $0.65\sigma_y$; (j) stress distribution in a diamond unit cell under compressive loading. Circles: cracks; square: pitting.

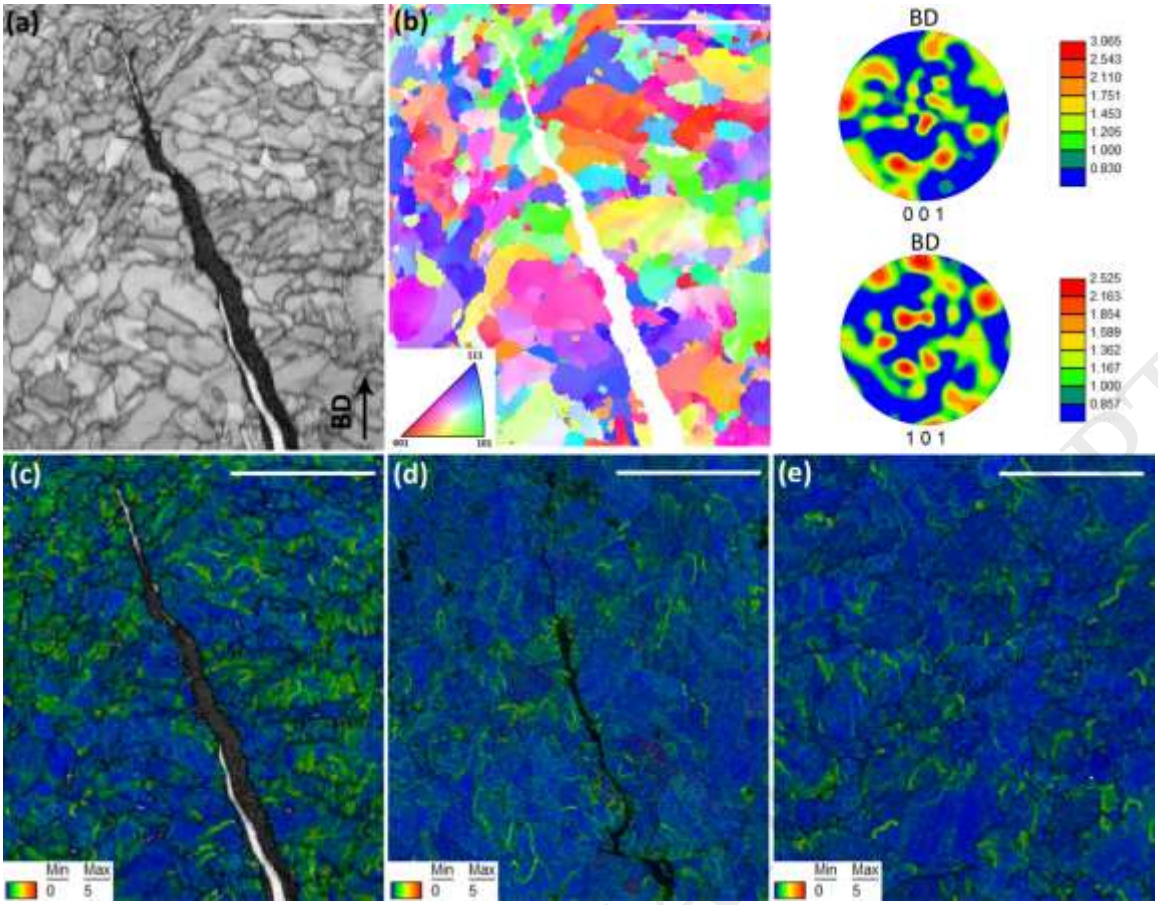

Figure 7. EBSD characterization of the fatigue crack track in air: (a) IQ map of the specimen tested at $0.9\sigma_y$; (b) IPF map of the specimen tested at $0.9\sigma_y$; (c) KAM map of the specimen tested at $0.9\sigma_y$; (d) KAM map of the specimen tested at $0.65\sigma_y$; (e) KAM map of the as-built sample. Scale bar: 25 μm.

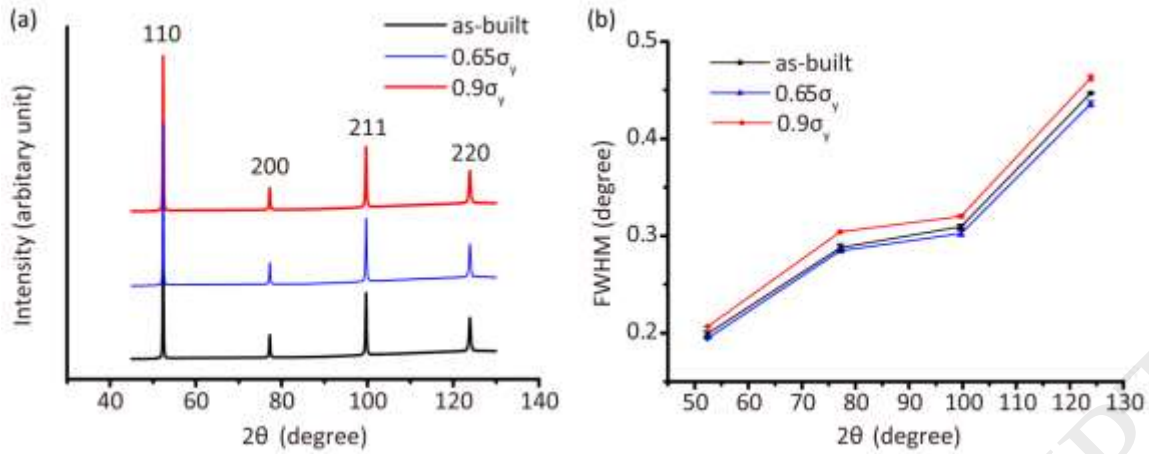

Figure 8. XRD analysis of the AM porous iron before and after the fatigue test in air at $0.9\sigma_y$: (a) XRD patterns; (b) FWHM.